Journal of *Marine Science and Engineering*

MDPI

Article

Room-Temperature Creep Deformation of a Pressure-Resistant Cylindrical Structure Made of Dissimilar Titanium Alloys

Zirui Liu [1], Fang Wang [1,*], Bingxiong Zhao [2], Jinfei Zhang [1], Oleg Gaidai [1], Zhongzhou Sun [1] and Kelin Wang [1]

[1] Shanghai Engineering Research Center of Hadal Science and Technology, College of Engineering Science and Technology, Shanghai Ocean University, Shanghai 201306, China
[2] Naval Architecture and Shipping College, Guangdong Ocean University, Zhanjiang 524088, China
* Correspondence: wangfang@shou.edu.cn

Abstract: The long-term safety of pressure-resistant structures used in deep-sea equipment may be threatened by creep deformation. The creep deformation behavior of a pressure-resistant structure made of different titanium alloys, Ti-6Al-4V and Ti-4Al-2V, at room temperature is investigated in this research. The kinetics and mechanisms underlying creep deformation in these materials is explained by proposing an improved constitutive model considering the effects of stress level, loading rate and environmental temperature field, offering crucial information for optimizing design parameters and guaranteeing the lifespan of the structure. Model parameters are determined for the two types of titanium alloys based on tensile creep testing results and validated through a simulation of the experimental process. In this study, a material creep model was used to predict the long-term deformation of large pressure-resistant titanium structures to ensure safe long-term operation. The safety factor used in the model is 1.5. Finite element analyses are conducted for the creep behavior of the pressure-resistant structure under real operating circumstances based on the creep constitutive model. The simulation predicts stress distribution, strain evolution, and deformation size over long periods of time by integrating complicated geometries, boundary conditions, and material characteristics. The present research can provide basic information for the local impacts of creep deformation on the inside of facilities, which helps refine design strategies to reduce possible damage risks.

Keywords: pressure-resistant structure; room-temperature creep; TC4-TA17 alloy; dissimilar titanium alloys

Citation: Liu, Z.; Wang, F.; Zhao, B.; Zhang, J.; Gaidai, O.; Sun, Z.; Wang, K. Room-Temperature Creep Deformation of a Pressure-Resistant Cylindrical Structure Made of Dissimilar Titanium Alloys. *J. Mar. Sci. Eng.* **2024**, *12*, 1419. https://doi.org/10.3390/jmse12081419

Academic Editor: Cristiano Fragassa

Received: 10 July 2024
Revised: 8 August 2024
Accepted: 14 August 2024
Published: 17 August 2024

1. Introduction

Pressure-resistant shells, which are crucial load-bearing structures and the foundation of deep-sea equipment, are subjected to high hydrostatic pressures. Structure design and construction are essential for the safe service of the equipment. The material used for these structures must have exceptional properties to withstand hazardous environmental conditions in order to meet service requirements [1]. Titanium alloys, such as Ti-6Al-4V and Ti-4Al-2V, are known for their excellent mechanical properties, including their high strength-to-weight ratio and good corrosion resistance. Notably, these alloys maintain a significant margin of ductility even after cooling, which is beneficial for their use in various structural applications [2]. However, a significant obstacle to maintaining the structural integrity and longevity of submersibles composed of various titanium alloys is the phenomenon of creep deformation, particularly for large-scale equipment that must remain underwater for extended periods of time for operations. Large-scale underwater detection equipment often has a cylindrical shell as its basic construction, with reinforcing ribs for workers and critical equipment. The strength and rigidity of the shell must be compatible in order to guarantee dependable functioning.

Previously, designers focused primarily on strength. However, as knowledge of room-temperature creep deformation has grown, the degree of shell deformation during extended underwater operations is linked to material choice. To assess the influence of these deformations on strength and possible effects on internal components, a typical large-scale deep-sea equipment is considered for the present study as shown in Figure 1.

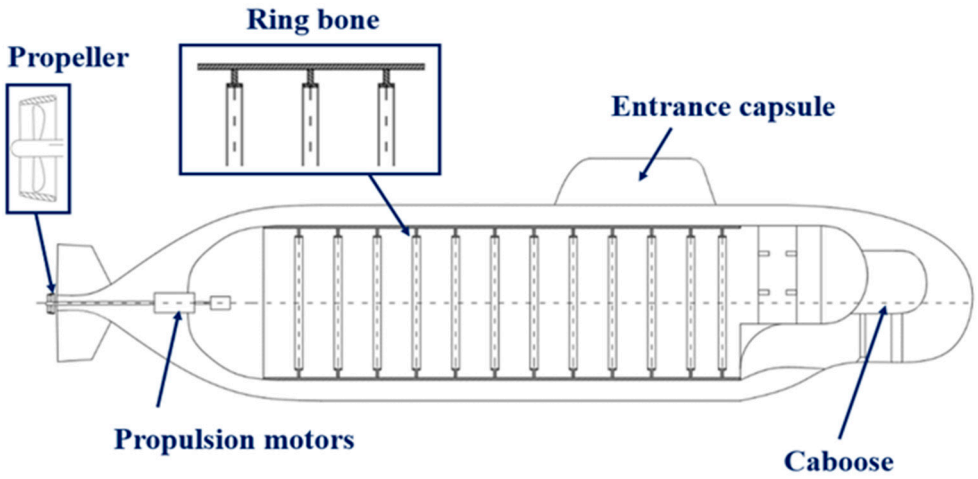

Figure 1. A schematic figure of large-scale deep-sea equipment.

Generally, cost concerns, corrosion resistance, and mechanical qualities must be carefully balanced when choosing titanium alloys for maritime applications. Ti-6Al-4V [3–7], Ti-10V-2Fe-3Al [8], and Ti-6Al-2Sn-4Zr-2Mo [9,10] are common titanium alloys, and each has its own advantages and trade-offs in terms of strength, ductility, and resistance to saltwater corrosion. The most prevalent material found in deep-sea equipment is Ti-6Al-4V. There are now enough studies [11] on Ti-6Al-4V pressure-resistant shells for deep-sea submersibles. In a medium-sized submersible design, Ti-6Al-4V is also considered to be the ideal material. Later on, the notion of combining two titanium alloys was put forth from the standpoint of cost reduction and efficiency enhancement against the background of the high cost of Ti-6Al-4V [11]. Lower-strength titanium alloys, such Ti-4Al-2V [12], are used to make ribs, primarily to increase rigidity, whereas higher-strength titanium alloys, like Ti-6Al-4V, are used to make shells. Usually, direct analysis techniques based on numerical simulation are used to calculate the performance of such structures.

In the context of continual load or stress, creep refers to the time-dependent plastic deformation of a material [13]. It is a complicated and multidimensional process that depends on a number of variables, including holding times [7,14,15], peak stress levels [10,16], microstructures [17–21], and stress ratios [14,22]. Currently, creep tests are frequently used to characterize the mechanical properties of materials [23,24]. Creep phenomena are typically studied under conditions associated with high temperatures [25–30]. However, creep at room temperature has attracted increasing attention in recent years with the advancement of deformation measurement technology due to its impact on structural reliability and safety, especially in applications where long-term stability is critical [31,32]. Localized deformations and stress concentrations can result from differential creep caused by stress, temperature, or microstructural differences within or across materials. These might ultimately jeopardize the structural integrity of the entire system. Thus, to lower the failure possibility of compressive constructions and to guarantee their long-term dependability, a thorough grasp of the creep behavior of several kinds of titanium alloys is necessary [33].

In this paper, a number of tests will be carried out to clarify the processes governing room-temperature creep for the two varieties of titanium alloys, Ti-6Al-4V and Ti-4Al-2V. In order to determine the elastic–plastic characteristics and creep damage model parameters of the material, respectively, the studies involve tensile tests on the material and creep tests conducted under controlled loading circumstances. Subsequently, the verified parameters

will be inserted into the pressure-resistant structure design to examine its creep behavior under real-world working conditions. This will be carried out by comparing the results of the experimental calculation with the results obtained from finite element analysis (FEA). The analysis will focus on the pressure-resistant structure's stress distribution, strain development, and probable failure mechanisms during an extended period of operation. Improvements in design parameters and material selection criteria can be guided by gaining valuable insights into the local impacts of creep inside the structure.

2. Materials and Structure

2.1. Material Properties

Ti-6Al-4V is an alpha–beta alloy, while Ti-4Al-2V is an alpha alloy. The ICP-AES spectrometer(Huacai Test Field, Luoyang, China), CS600 carbon and sulfur analyzer(Huacai Test Field, Luoyang, China), and other tools were used to determine the chemical compositions of Ti-6Al-4V and Ti-4Al-2V. The results are displayed in Table 1.

Table 1. Chemical composition of Ti-6Al-4V and Ti-4Al-2V alloys (wt%).

Materials	Element								
	Al	V	Fe	C	N	H	O	Si	Ti
Ti-6Al-4V	6.0	4.1	0.16	0.02	0.01	0.002	0.15	—	Base
Ti-4Al-2V	4.1	2.1	0.14	0.02	0.02	0.003	0.13	0.02	Base

The material properties of Ti-6Al-4V are referred to the experimental test values in previously published papers [7]. The quasi-static tensile test of the Ti-4Al-2V titanium alloy was carried out using a cylindrical specimen with a diameter of 6 mm × a length of 42 mm, according to GB/T 2039-2012 [34]. A static tensile test was carried out to obtain the properties of the material at room temperature, the results of which can be seen in Table 2 and Figure 2.

Table 2. Mechanical properties of Ti-6Al-4V and Ti-4Al-2V alloys.

Materials	Mechanical Property			
	E (GPa)	v	σ_s (MPa)	σ_b (MPa)
Ti-6Al-4V	110	0.3	850	916
Ti-4Al-2V	108	0.3	648	749

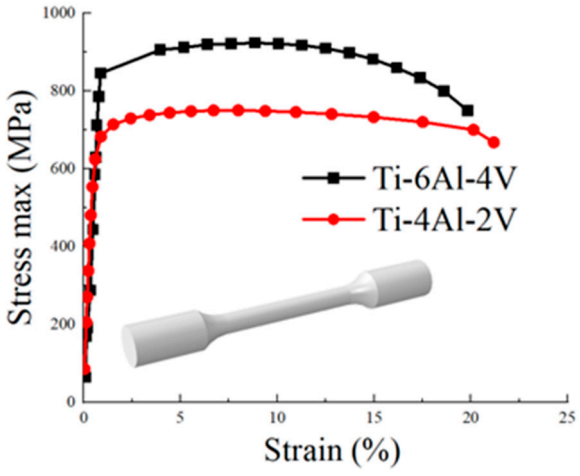

Figure 2. Stress–strain curves of Ti-6Al-4V and Ti-4Al-2V titanium alloys.

As seen in Figure 3, a uniaxial tensile creep test is carried out at room temperature on a cylindrical smooth specimen with dimensions of 5 mm (diameter) × 27 mm (length) using an electronic creep fatigue testing equipment, QBR-100 (Huacai Test Field, Luoyang, China). In our study, we adhered to the ASTM E139-11 [35] standards for conducting creep testing. Tensile creep testing consists of two stages including the loading stage and the load-sustaining stage. An axial extensometer is used to measure the axial strain at each step.

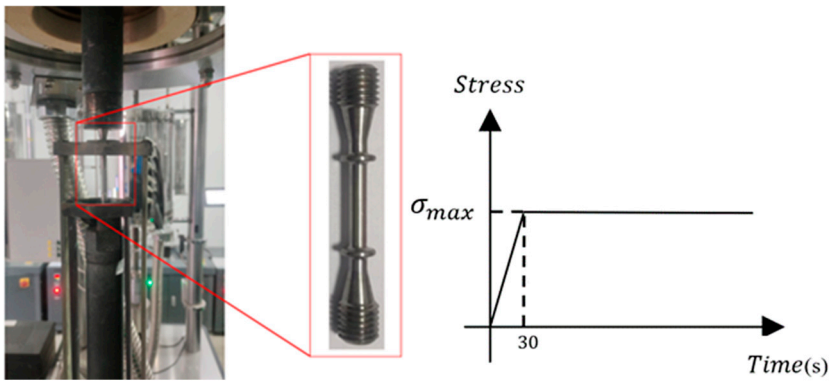

Figure 3. Room-temperature tensile creep test.

The creep stress levels and load-sustaining time for the room-temperature tensile creep tests are chosen as shown in Table 3 based on the levels of yield strength σ_s of the two materials. In order to avoid the difficulties of data dispersion in the creep testing of titanium alloys, we tested multiple specimens in each group according to the stress criteria in Table 3 during testing. The results were analyzed statistically in a comprehensive manner and the mean values were selected for processing.

Table 3. Room-temperature creep test conditions.

σ_{max}/σ_s	0.85	0.90	0.905	0.92	0.95	0.958	0.976
Ti-6Al-4V	/	/	300,000 s	300,000 s	/	150,000 s	50,000 s
Ti-4Al-2V	300,000 s	300,000 s	/	300,000 s	300,000 s	/	/

The total strain produced over time is measured during the creep tests and compared to assess the effects of loading at different yield strength ratios on creep deformation. Eight specimens in all are machined in a direction parallel to the rolling direction for sampling, and the tester's extensometer records the deformation data every ten minutes. Figure 4 displays the test results at the end.

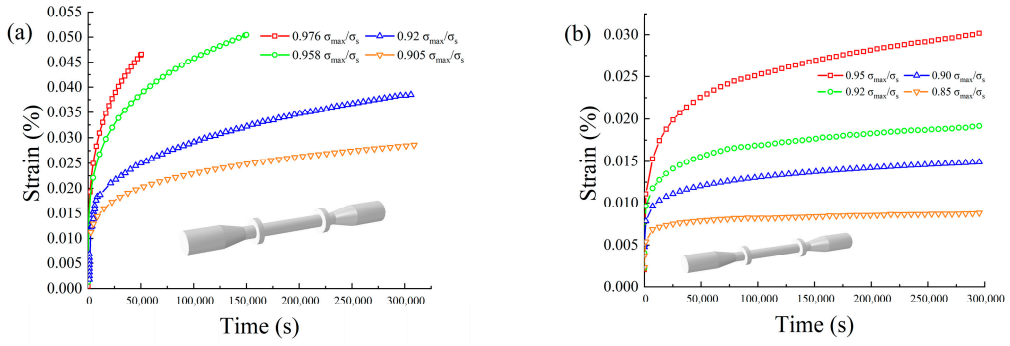

Figure 4. Room-temperature creep deformation curves of the alloys: (**a**) Ti-6Al-4V; (**b**) Ti-4Al-2V.

2.2. Structure Form

The load-bearing capability of the deep-sea equipment should be in accordance with the operating environment. The calculation model for the pressure-resistant structure in the present study can be divided into two parts, namely, the cylindrical shell and the ribs. The specific dimensions of the structure are given in Table 4 and the geometry is shown in Figure 5. The goals are to investigate the differences between the pressure-resistant structure composed of dissimilar materials and the traditional Ti-6Al-4V pressure-resistant structure, to verify the reliability of the dissimilar material's pressure-resistant structure, and to lower the cost for the construction of large-scale underwater submersibles.

Table 4. Parameters of deep-sea pressure-resistant structure.

Item	Value
Pressure-resistant shell inner diameter (Ti-6Al-4V)	424 mm
Initial wall thickness	26 mm
T-beam height (Ti-4Al-2V)	116 mm
T-beam width (Ti-4Al-2V)	70 mm
T-beam wing (Ti-4Al-2V)	16 mm
T-beam web (Ti-4Al-2V)	14 mm
T-beam spacing	200 mm

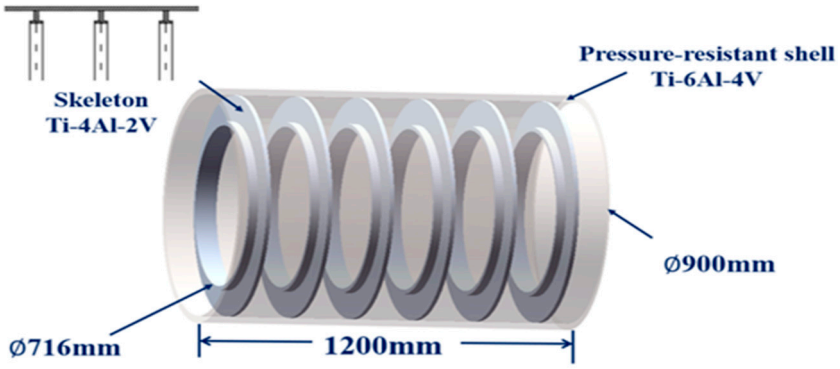

Figure 5. The structure form of the pressure-resistant structure.

3. Creep Constitutive Model

When doing finite element analysis, three types of creep models are typically used: the hyperbolic sine model, the strain-hardening model, and the age-hardening model. Of these, the hyperbolic sine law model is often used for creep characteristics under changing temperature settings, and the strain-hardening model or age-hardening model are chosen for creep properties under constant temperature and load-sustaining situations. While the structural creep parameters of deep-sea equipment working for extended periods of time have a substantial relationship with time, the strain-hardening model is appropriate for short-term tests since it makes the assumption that creep deformation has no relationship with time. Based on uniaxial tensile creep test results, an age-hardening creep-strain-rate constitutive model for the room-temperature titanium alloys Ti-6Al-4V and Ti-4Al-2V is proposed as follows:

$$\Phi(\dot{\varepsilon}_{cr}, \sigma, t) = 0 \tag{1}$$

$$\begin{cases} \varepsilon_{cr} = f_1(\sigma) f_2(t) \\ f_1(\sigma) = \sigma^n \\ f_2(t) = \frac{A}{m+1} t^{m+1} \end{cases} \tag{2}$$

where m is the time order parameter (it should be emphasized that the time order parameter must be negative), $\dot{\varepsilon}_{cr}$ is the uniaxial creep strain rate, $f_1(\sigma)$ is the stress function, n is the equivalent stress order parameter, $f_2(t)$ is the time response function, A is the power

law multiplier parameter, and $f_2(t)$ is the time response function. Integration can place the strain model in a three-dimensional stress state, which is provided by the following equation. The uniaxial creep strain rate $\dot{\varepsilon}$ is the first-order derivative of the total uniaxial creep deformation ε at time t,

$$\varepsilon_{cr} = \frac{A}{m+1} \cdot \sigma^n \cdot t^{m+1} + C \tag{3}$$

where C is the material constant and ε_{cr} is the total uniaxial creep deformation.

Taking logarithms on both sides of Equation (3),

$$\ln \varepsilon = \ln \frac{A}{m+1} + \mathrm{n} \ln \sigma + (\mathrm{m}+1) \ln \mathrm{t} + \ln \mathrm{C} \tag{4}$$

The curves of $ln\varepsilon \sim lnt$ and $ln\sigma \sim ln\varepsilon$ are significant in A, n, m fitting, according to Equation (4). By using distinct ε and σ data in Equation (4) and carrying out approximate elimination, it is possible to fit the value of n by using Equation (5),

$$\ln \varepsilon_1 - \ln \varepsilon_2 = \mathrm{n}(\ln \sigma_1 - \ln \sigma_2) \tag{5}$$

The A, n, and m parameters of the Norton–Bailey equation fitted through Equation (5) are shown in Table 5.

Table 5. Norton-Bailey model parameters of Ti-6Al-4V, Ti-4Al-2V alloys.

Materials	Model Parameters		
	A	***n***	***m***
Ti-6Al-4V	4.2×10^{-49}	15.5	-7.35×10^{-1}
Ti-4Al-2V	7.20×10^{-27}	8.2	-8.54×10^{-1}

Material constant C, which is determined as indicated by Equation (11) and is the total strain difference between the creep damage mechanical model integration and the elastic strain that results from the application of the axial loading force to the specimen, is influenced by the mechanical properties of the material itself.

$$\mathrm{C} = \frac{A}{m+1} \sigma^n t_a^{m+1} - \varepsilon_a \tag{6}$$

where ε_a is the elastic strain that happened in 30 s, and t_a is the loading completion time, which is 30 s based on Figure 3. The calculated C values are shown in Table 6 below.

Table 6. Material parameter C-fit processing of Ti-6AL-4V, Ti-4AL-2V alloys.

σ_{max}/σ_s	**0.85**	**0.90**	**0.905**	**0.92**	**0.95**	**0.958**	**0.976**
Ti-6Al-4V	/	/	4.03×10^{-3}	4.16×10^{-3}	/	2.18×10^{-3}	-2.15×10^{-4}
Ti-4Al-2V	-1.13×10^{-3}	-2.73×10^{-3}	/	9.51×10^{-4}	5.04×10^{-3}	/	/

The obtained Norton–Bailey model parameters were obtained by fitting the curve as shown in Figure 6. Since the Norton–Bailey model is mainly applied to the second stage of creep, the correlation coefficient was verified to be 92% by Matlab 2020, and in order to more accurately fit the experimental curves, we made further observations on the introduced parameters. Upon examining the $ln\varepsilon \sim lnt$ and $ln\sigma \sim ln\varepsilon$ curves, it is seen that A and m + 1 are similarly altered as the peak stress rises, as shown in Figure 7. In conjunction with the value of n derived from Equation (5), the following stress-related time-hardening model can be put forth:

$$\varepsilon_{cr} = \frac{A_\sigma}{m_\sigma + 1}\sigma^n t^{m_a+1} + C \tag{7}$$

$$\begin{cases} A_\sigma = a_A\sigma + b_A \\ m_\sigma + 1 = a_m\sigma + b_m \end{cases} \tag{8}$$

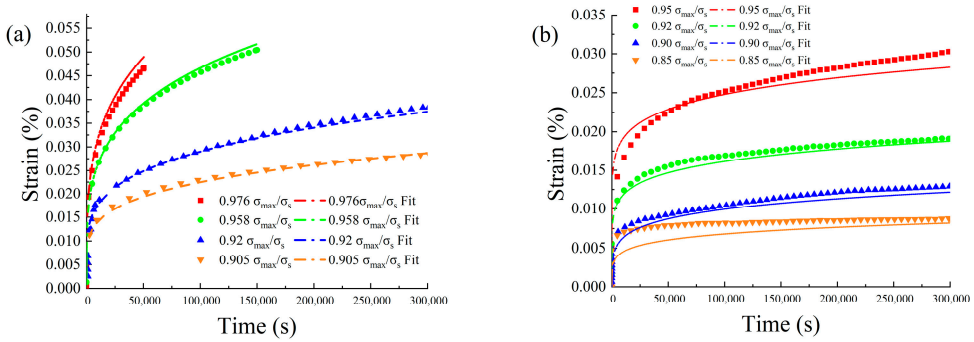

Figure 6. Comparison of fitting results and test data: (**a**) Ti-6Al-4V; (**b**) Ti-4Al-2V(Norton–Bailey).

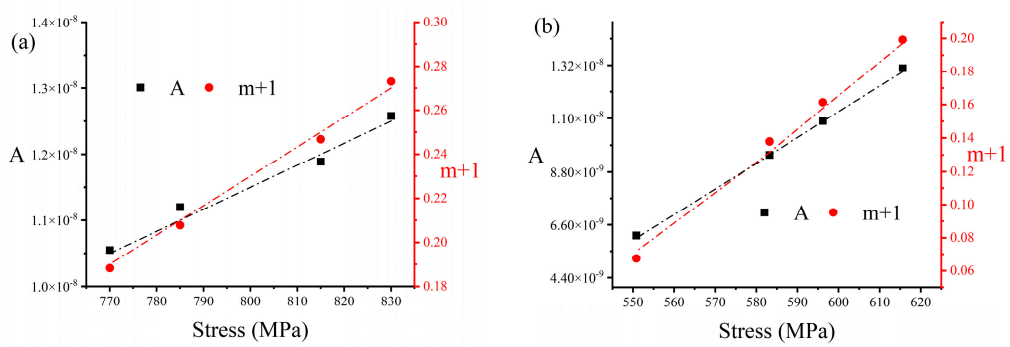

Figure 7. Norton–Bailey's parameter A with m + 1: (**a**) Ti-6Al-4V; (**b**) Ti-4Al-2V.

The creep test data for the maximum peak stress loading and minimum peak stress loading of the Ti-6Al-4V and Ti-4Al-2V titanium alloys, respectively, at room temperature were substituted into Equation (6). The data were then fitted and the error of the correlation coefficient was greater than 0.99. The fitted data are displayed in Table 7. Nevertheless, as seen in Equation (8), the time order parameter has a comparable interval constraint because of the power law multiplier parameter.

$$\begin{cases} A > 0 \\ 1 > m + 1 > 0 \end{cases} \tag{9}$$

Table 7. The creep constitutive model parameters of Ti-6Al-4V and Ti-4Al-2V alloys.

Materials	Model Parameters				
	a_A	b_A	a_m	b_m	n
Ti-6Al-4V	3.33×10^{-11}	-1.52×10^{-8}	1.33×10^{-3}	-8.37×10^{-1}	1.62
Ti-4Al-2V	1.39×10^{-10}	-7.14×10^{-8}	1.55×10^{-3}	-7.71×10^{-1}	1.65

By replacing the values of a_A, b_A, a_m, and b_m from Equations (7) and (8) with the values obtained from Table 5, a tolerable stress range for the model may be established as follows:

$$\begin{cases} a_A\sigma + b_A > 0 \\ 1 > a_m\sigma + b_m > 0 \end{cases} \tag{10}$$

$$\begin{cases} \sigma > -\frac{b_A}{a_A} \\ 1 > a_m\sigma + b_m > 0 \\ \sigma \leq \sigma_s \end{cases} \tag{11}$$

The customized subroutine of the creep constitutive model for the two materials may be used in the finite element analysis of the structure by synthesizing the intervals of Equation (10). Ultimately, it was confirmed that the applicability ranges for parameter A for Ti-6Al-4V are 457 MPa~850 MPa. The range of parameter $m + 1$ is 628 MPa~850 MPa. The applicability ranges for parameter A for Ti-4Al-2V are 514 MPa~648 MPa and the applicability ranges for parameters $m + 1$ are 500 MPa~648 MPa.

As can be observed in Table 7, which shows all the data sets concerning material constant C after processing and analysis, material constant C steadily declines as peak stress increases, demonstrating that the fitted value of the model is closer to the actual test data. Since only two groups of data, the maximum peak stress and the minimum peak stress, are used to fit the parameters of the creep damage mechanical model, but the fitting errors obtained for the total four groups of data do not exceed 1%, this indicates the validity and reliability of the model, as demonstrated in Figure 8. By comparing the data obtained from the creep constitutive model parameters in Tables 7 and 8 with the data obtained from the uniaxial tensile creep tests at room temperature, it can be seen that the fitting results agree well with the test data.

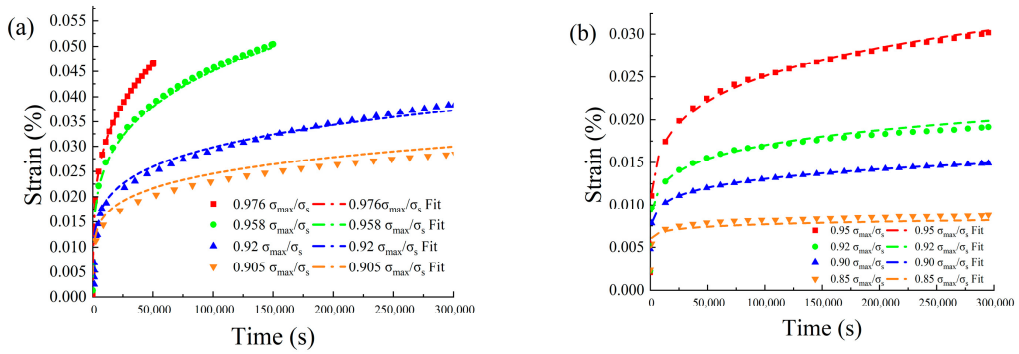

Figure 8. Comparison of fitting results and test data: (**a**) Ti-6Al-4V; (**b**) Ti-4Al-2V (improved linear model).

Table 8. Material parameter C-fit processing of Ti-6AL-4V and Ti-4AL-2V alloys.

σ_{max}/σ_s	**0.85**	**0.90**	**0.905**	**0.92**	**0.95**	**0.958**	**0.976**
Ti-6Al-4V	/	/	1.17×10^{-3}	1.06×10^{-3}	/	6.95×10^{-4}	4.46×10^{-4}
Ti-4Al-2V	2.34×10^{-3}	9.92×10^{-4}	/	7.83×10^{-4}	1.98×10^{-4}	/	/

4. Finite Element Analysis

4.1. Model Validation

Utilizing the commercial software ABAQUS 2020, the corresponding finite element model is established in accordance with the dimensions of the specimen of the room-temperature tensile creep test, allowing for the verification of the accuracy of the creep constitutive model. Because of the restrictions' symmetry with regard to the central axis, the one-quarter model is used. As seen in Figure 9, the *xoy* plane has symmetric constraints set in the positive direction of the Z-axis, $U_z = UR_x = UR_y = 0$, and the *yoz* plane has symmetric constraints set in the positive direction of the X-axis, $U_x = UR_y = UR_z = 0$. The end face of the tensile model's negative Y-axis side is fixed, $U_x = U_y = U_z = UR_x = UR_y = UR_z = 0$, to avoid the possibility of stiff body motion. Then, a creep damage model subroutine is applied as the input based on the fitted parameters. The same condition as that in the tensile creep test is applied to the calculation.

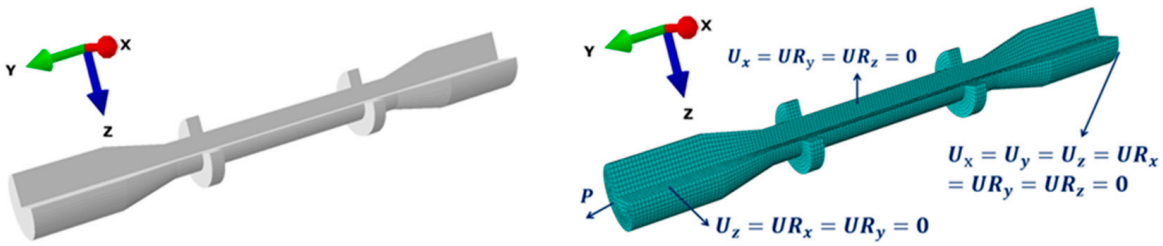

Figure 9. Finite element model of the specimen.

The creep deformation curves with time for the specimens are given in Figure 10. The suggested creep constitutive model and model parameters are validated to be accurate by comparing the results from the finite element simulation and the test data.

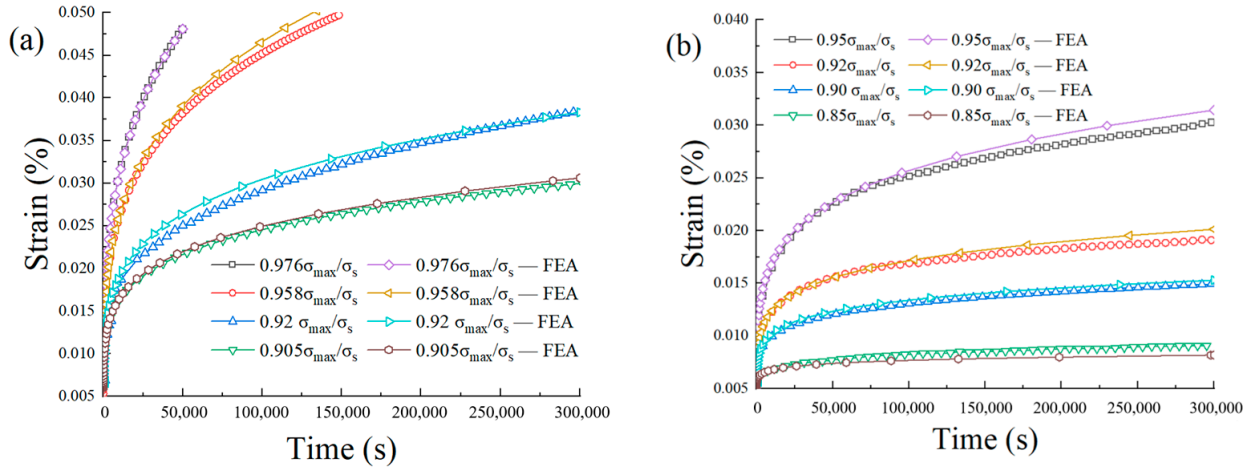

Figure 10. Comparison of creep deformation between simulation results and test data: (**a**) Ti-6Al-4V; (**b**) Ti-4Al-2V.

4.2. Analysis on Pressure-Resistant Cylindrical Shell

The creep deformation of the pressure-resistant structure presented in Figure 5 is analyzed by finite element simulation in this section. A water depth of 3000 m, or a hydrostatic pressure of 30 MPa, is assumed for analysis. This is the normal operating depth of a large-scale underwater exploration station. As shown in Figure 3, the loading mode is applied gradually from 0 MPa to 30 MPa at a loading rate of 1 MPa/s. After that, the loading is maintained at 30 MPa. A one-year time period was represented by setting the time duration of the viscous analysis to 3.1536×10^7 s and enabling geometric nonlinearity. On the *xoy* plane, $U_z = UR_x = UR_y = 0$ symmetric constraint is imposed in the positive direction of the *Z*-axis, and on the *yoz* plane, a symmetric constraint is imposed, $U_x = UR_y = UR_z = 0$, in the positive direction of the *X*-axis. The pressure-resistant structural model's end faces, $U_x = U_y = U_z = UR_x = UR_y = UR_z = 0$, on each side of the *Y*-axis, are locked in order to prevent stiff body motion. The loading force direction and boundary conditions are established as illustrated in Figure 11, and the maximum uniform pressure $p_0 = 30$ MPa is applied to the model's shell surface to simulate the hydrostatic pressure beneath 3000 m in the room-temperature test environment.

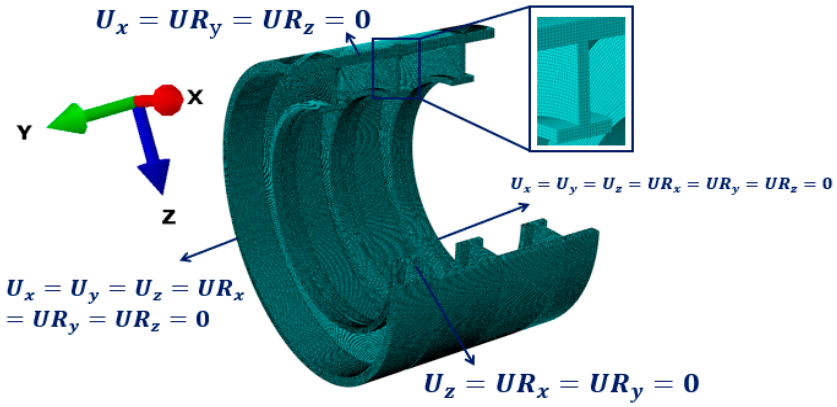

Figure 11. Finite element model of the pressure-resistant cylindrical shell with boundary conditions.

4.2.1. Mesh Convergence Analysis

Mesh sizes of 2 mm, 4 mm, 8 mm, and 16 mm are selected as multiples of 2 as indicated in Figure 12 for mesh convergence analysis. The equivalent creep strain are displayed in Figure 13 at different mesh densities, where it is evident that the equivalent creep strain grows along with the mesh density. The midpoint of the *xoy* surface in the *Z*-axis direction of the ring-ribbed cylindrical shell and the midpoint of the mid-rib plate in the *Z*-axis direction of the T-rib plate, as shown in Figures 14–16, are used to analyze the maximum stress, displacement, and strain under various mesh densities. The findings demonstrate that the T-ribbed plate and the ring-ribbed column shell's *Y*-axis stresses tend to stabilize with time and that the higher the mesh density, the more beneficial the stress propagation. However, it is discovered that the mesh density of 16 mm is unable to properly transmit the displacement deformation. Therefore, it is not taken into consideration when the *Y*-axis displacement of the T-rib plate and ring-ribbed column shell is examined. In terms of strain, the higher the mesh density, the more beneficial the strain propagation becomes as the same load grows over time. As can be seen in Table 9, different mesh densities under the number of meshes and displacement error coefficients result in very small errors for 2 mm and 4 mm displacements. Therefore, selecting a 4 mm mesh density for the creep calculation of pressure-resistant structures is a reasonable and effective way to save finite element calculation work.

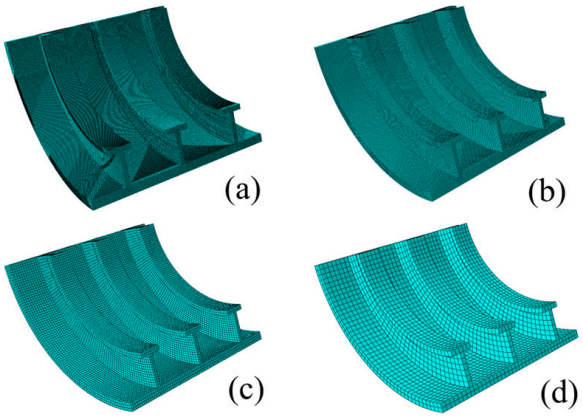

Figure 12. Modeling of pressure-resistant structures with different meshes density: (**a**) mesh density = 2 mm; (**b**) mesh density = 4 mm; (**c**) mesh density = 8 mm; (**d**) mesh density = 16 mm.

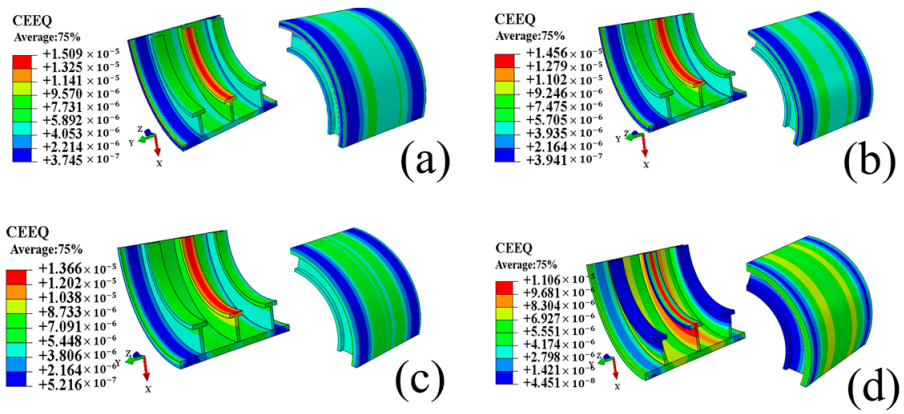

Figure 13. Equivalent creep for different mesh densities: (**a**) mesh density = 2 mm; (**b**) mesh density = 4 mm; (**c**) mesh density = 8 mm; (**d**) mesh density = 16 mm.

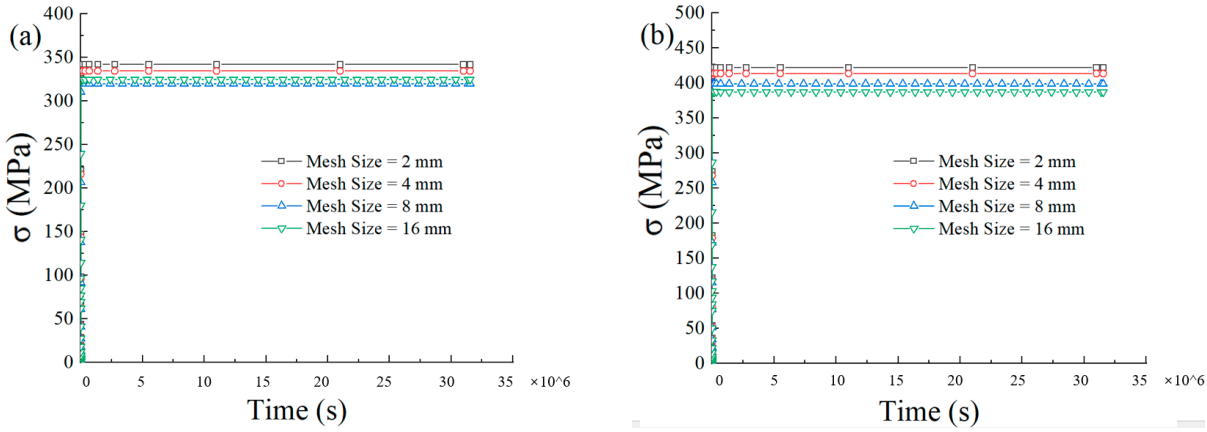

Figure 14. Variation curves of maximum stress values for different mesh densities: (**a**) annular column shell; (**b**) T-ribbed flange.

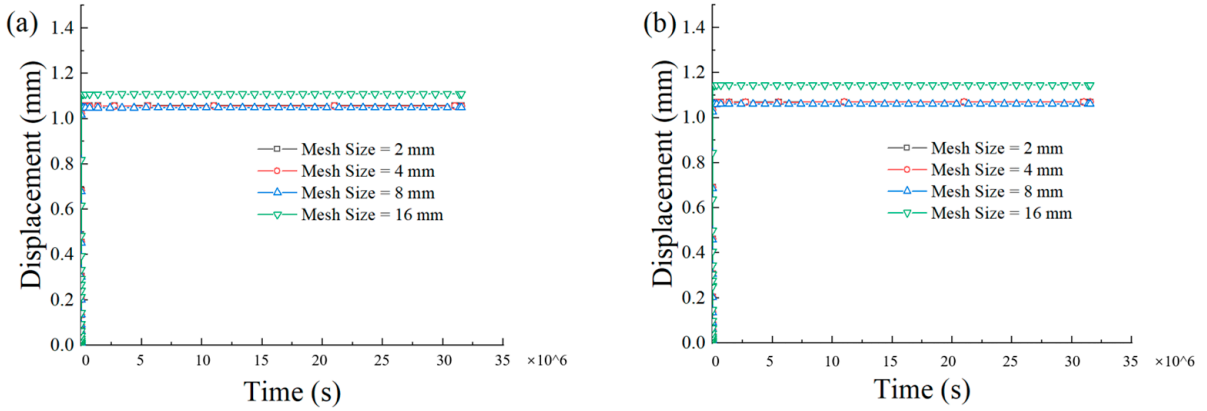

Figure 15. Variation curves of displacement for different mesh densities: (**a**) annular column shell; (**b**) T-ribbed flange.

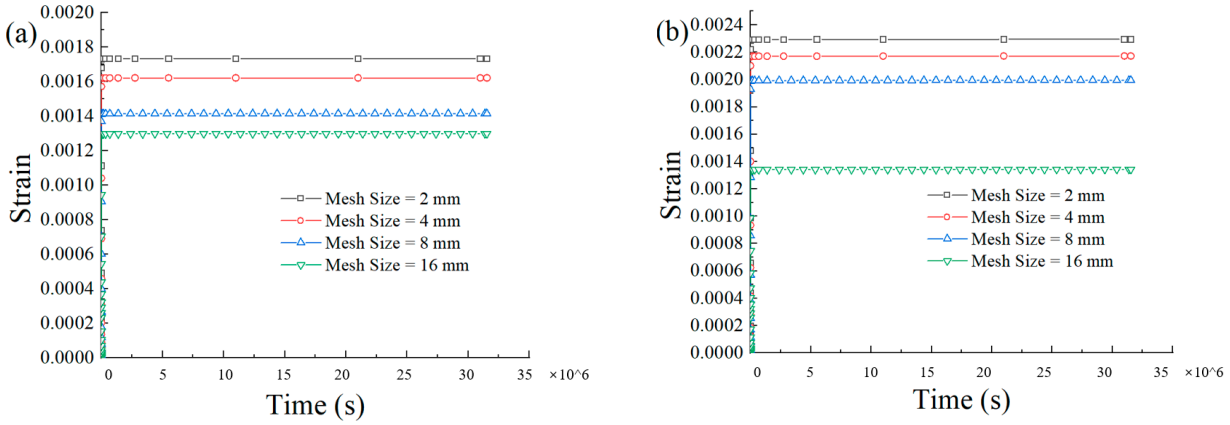

Figure 16. Variation curves of strain for different mesh densities: (**a**) annular column shell; (**b**) T-ribbed flange.

Table 9. Finite element simulation results corresponding to different mesh pressure-resistant structures.

Composition	Ring-Ribbed Column Shell			T-Ribbed Flange		
Mesh Size	***Elem Number***	***Displacement***	***Relative Error***	***Elem Number***	***Displacement***	***Relative Error***
2 mm	1,338,246	1.238 mm	0.08%	546,300	1.260 mm	0.08%
4 mm	181,944	1.237 mm	—	69,536	1.259 mm	—
8 mm	19,380	1.229 mm	0.97%	8970/	1.250 mm	0.71%
16 mm	3354	1.366 mm	10.43%	1122/	1.758 mm	39.63%

4.2.2. Effect of Load Magnitude on Creep in the Pressure-Resistant Structure

Before analyzing the load magnitude effect, the ultimate strength of the structure is calculated for the determination of the pressure range. A numerical analysis of the pressure-resistant structure's linear buckling (eigenvalues) and nonlinear buckling (Riks) yields the maximum critical load of 76.5 MPa, and its load–displacement curve is displayed in Figure 17.

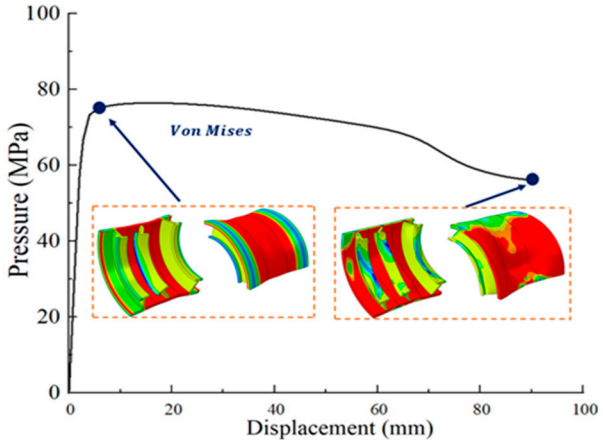

Figure 17. Load–displacement curves for pressure-resistant structures.

A variety of working conditions affecting creep properties of the structure are provided in Table 10 according to distinct circumstances. As the maximum load was determined to be 76.5 MPa, the maximum load in the finite element simulation should not exceed 51.2 MPa. The equivalent creep simulation results are displayed in Figure 18, which demonstrates that the equivalent creep strain increases significantly as the loaded loads increase.

Table 10. Factors affecting deep and shallow working conditions in the oceans.

Depths (m)	Pressure (MPa)	Temperature (°C)
2500	25	3.5
3000	30	2
3500	35	1.5
4000	40	1
5000	50	0

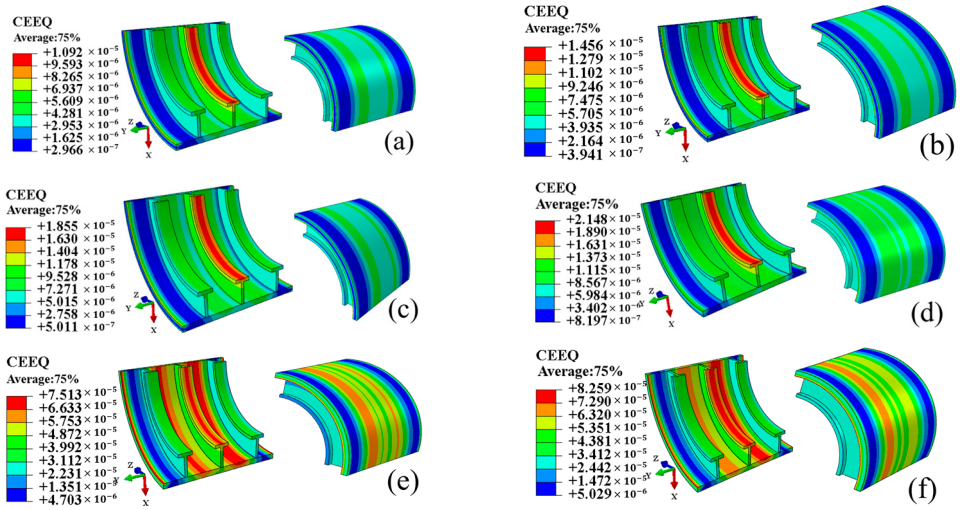

Figure 18. Equivalent creep for different load magnitude: (**a**) loading = 25 MPa; (**b**) loading = 30 MPa; (**c**) loading = 35 MPa; (**d**) loading = 40 MPa; (**e**) loading = 45 MPa; (**f**) loading = 50 MPa.

As seen in Figures 19–21, its maximum stress, displacement, and strain under various loading pressures is studied. The findings demonstrate that, in the range of 25 MPa to 50 MPa, the *Y*-axis stresses, displacements, and strains of the T-ribbed plate and the ring-ribbed column shell tend to rise with an increase in applied pressure and converge steadily over time. In addition to the obvious initial elastic displacement of the pressure-resistant structure after the initial application of load, the creep displacement in the working environment of one year can be seen in Figure 22 and Table 11, and the displacement change is microscopic for the whole structure. The preselected preset conditions grow with the application of load to simulate the underwater environment of 2500 m to 5000 m of the deep sea. The results show that the use of structures made of two different metal materials, Ti-6Al-4V and Ti-4Al-2V, can meet the work intensity of replacing the pure Ti-6Al-4V structure and reduce the cost of offshore equipment.

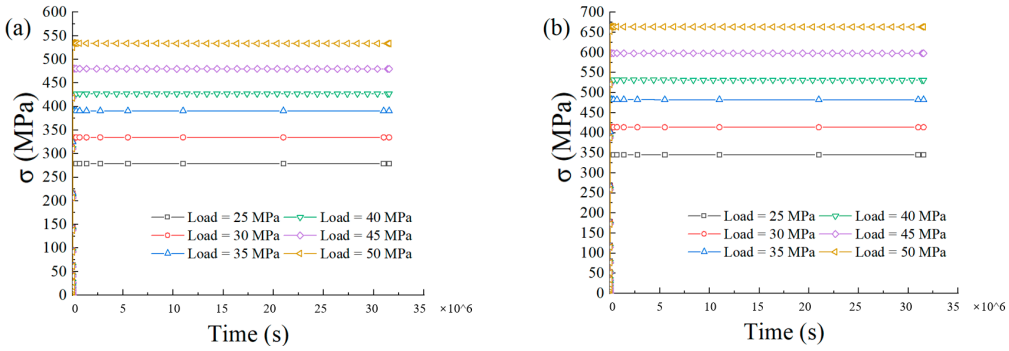

Figure 19. Variation curves of maximum stress values for different load magnitudes: (**a**) annular column shell; (**b**) T-ribbed flange.

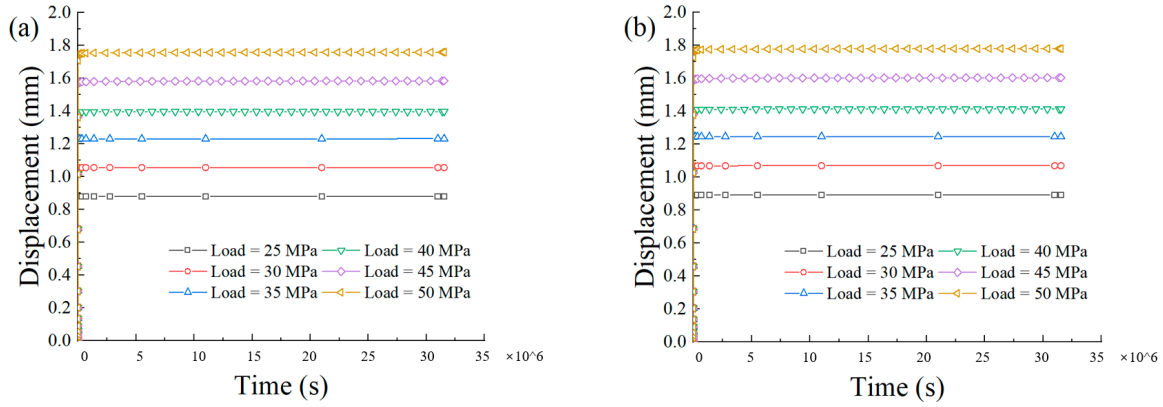

Figure 20. Variation curves of displacement for different load magnitudes: (**a**) annular column shell; (**b**) T-ribbed flange.

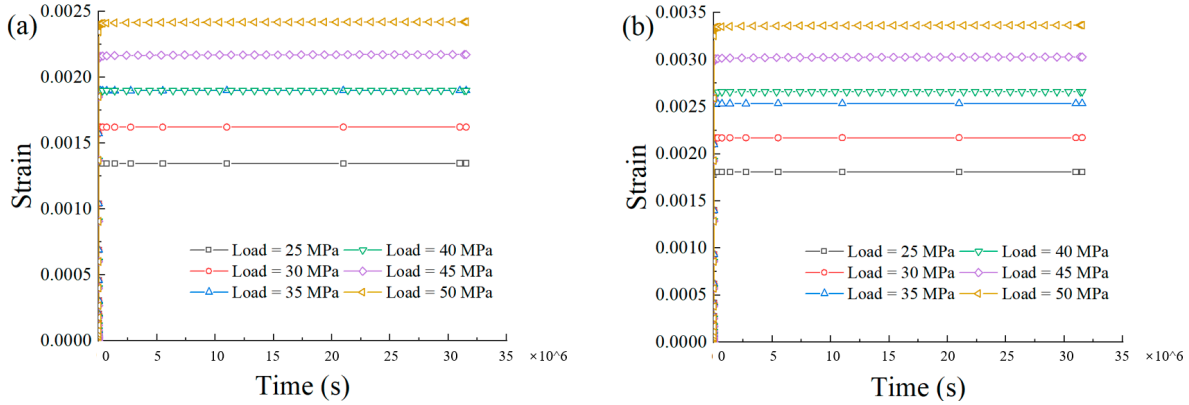

Figure 21. Variation curves of strain for different load magnitudes: (**a**) annular column shell; (**b**) T-ribbed flange.

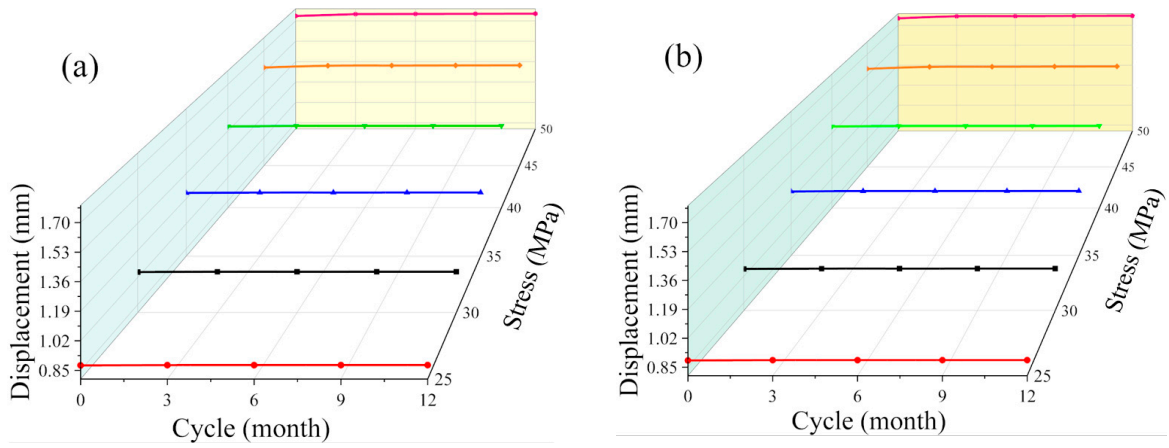

Figure 22. Displacement variation curves at different time periods: (**a**) Ti-6Al-4V; (**b**) Ti-4Al-2V.

Table 11. Displacement over time.

Materials	Pressure (MPa) Cycle (Month)	25	30	35	40	45	50
		Displacement (mm)					
Ti-6Al-4V	**Tensile**	0.8787	1.05385	1.2288	1.39364	1.56691	1.73997
	3	0.88017	1.0558	1.23127	1.39675	1.58086	1.75548
	6	0.88026	1.05592	1.23143	1.39708	1.58237	1.75711
	9	0.88035	1.05604	1.23158	1.39729	1.58336	1.75818
	12	0.88049	1.05622	1.23181	1.3975	1.58443	1.75922
Ti-4Al-2V	**Tensile**	0.88968	1.06696	1.24401	1.40902	1.56691	1.73997
	3	0.89138	1.06921	1.24686	1.41258	1.59971	1.7764
	6	0.89148	1.06934	1.24704	1.41295	1.6014	1.77823
	9	0.89158	1.06948	1.24722	1.4132	1.6025	1.77943
	12	0.89173	1.06969	1.24748	1.41344	1.60358	1.78059

4.2.3. Effect of Loading Rate on Creep of the Pressure-Resistant Structure

The pressure on the structure model was eventually loaded to 30 MPa and maintained for one year by adopting four different loading rates of 0.5 MPa/s, 1 MPa/s, 2 MPa/s, and 5 MPa/s. Its equivalent creep is shown in Figure 23, where it is evident that as the loading rate increases, the equivalent creep also increases significantly. Figures 24–26 display the maximum stress, displacement, and strain curves at the midpoint of the T-ribbed plate and ring-ribbed cylindrical shell at various loading rates (the chosen locations are the same as in Section 4.2.1). The key factor causing the variation in loading times is the loading rate; the lower the loading rate, the longer the loading time. All four loading rates were loaded at 30 MPa. It is evident from Figure 24 that the pressure-resistant structure's Y-axis displacements have a tendency to stabilize. It is evident that, during both the loading and load-sustaining phases, there are very few variations in the displacement values for the four distinct loading rates. For the same holding, loading time displacements rise as the loading rate increases. Using 0.5 MPa/s as the reference point, the displacement at 0.5 MPa/s and 5 MPa/s loading rates are 1.06954 mm and 1.06999 mm, respectively, with a 0.04% error factor. As a result, in order to maintain the pressure-resistant structure in the high-pressure environment of creep strain and displacement release, the loading process and the amplitude must acknowledged. Based on the creep specimen loading time shown in Figure 3, the pressure-resistant structure that was ultimately selected for the finite element calculation of creep loading for 1 MPa / s is similar to the large structure's loading time.

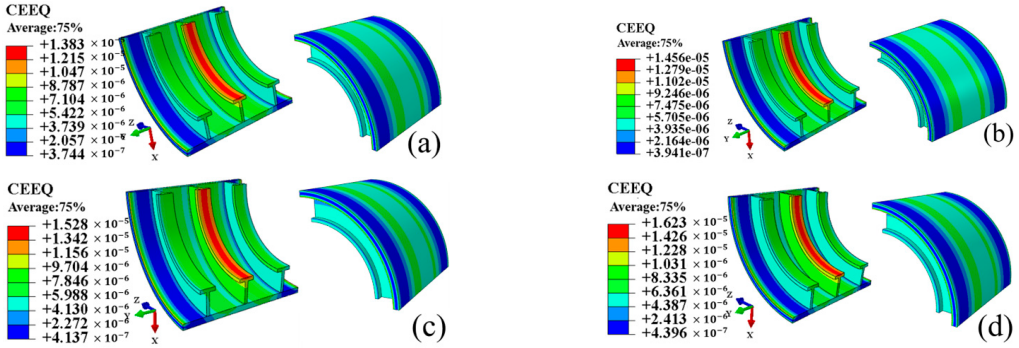

Figure 23. Equivalent creep for different loading rates: (**a**) rate = 0.5 MPa/s; (**b**) rate =1 MPa/s; (**c**) rate = 2 MPa/s; (**d**) rate = 5 MPa/s.

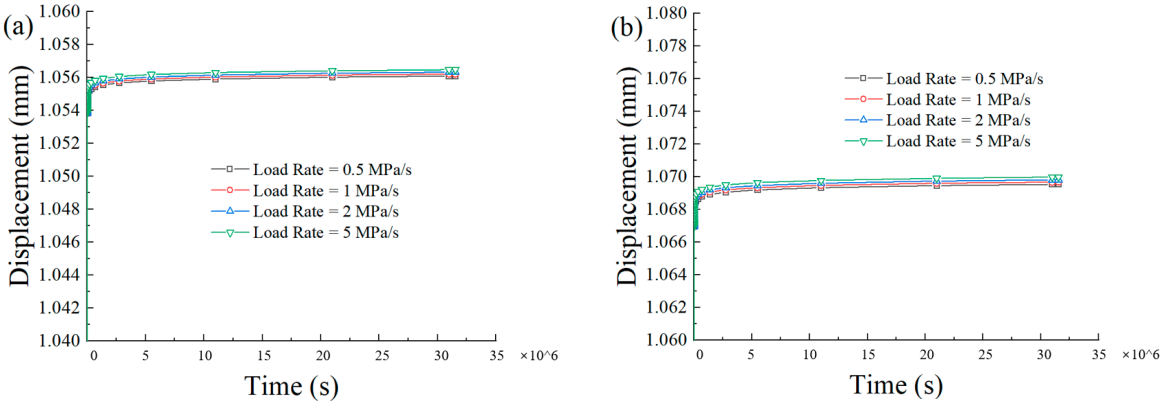

Figure 24. Variation curves of displacement for different load rates: (**a**) annular column shell; (**b**) T-ribbed flange.

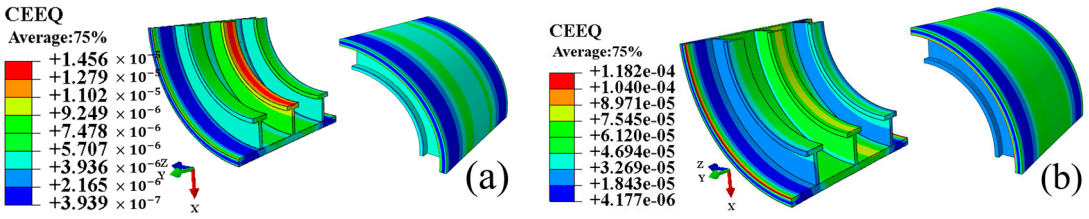

Figure 25. Equivalent creep strain for different loads with initial geometric imperfection: (**a**) 30 MPa; (**b**) 50 MPa.

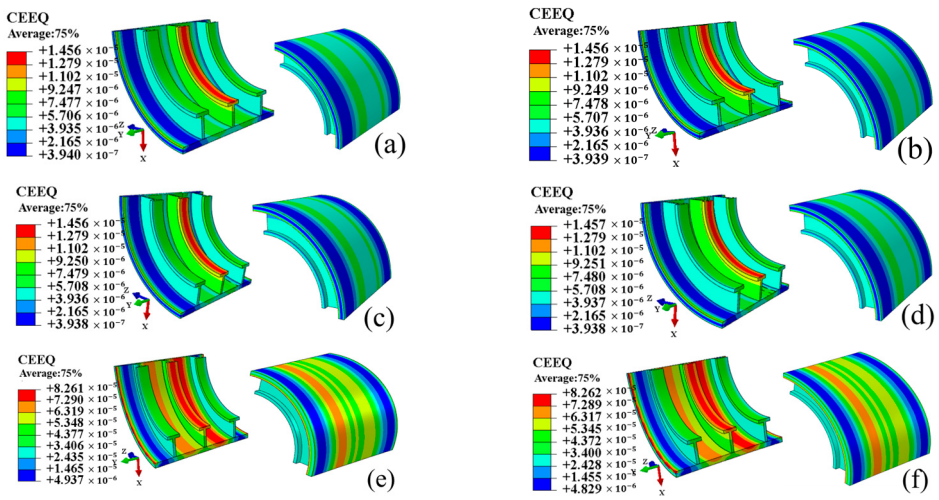

Figure 26. Equivalent creep for different initial geometric imperfections: (**a**) imperfection = 1 mm, 30 MPa; (**b**) imperfection = 2 mm, 30 MPa; (**c**) imperfection = 3 mm, 30 MPa; (**d**) imperfection = 4 mm, 30 MPa; (**e**) imperfection = 2 mm, 50 MPa; (**f**) imperfection = 4 mm, 50 MPa.

4.2.4. Effect of Initial Geometric Imperfection on Creep of the Pressure-Resistant Structure

The normal maximum stresses, displacements, and strains under 30 MPa and 50 MPa displacements under the initial conditions with initial geometric defects were taken for comparison (i.e., manufacturing defects were taken as five-thousandths of the inside diameter, 5‰Ri). Initial geometric imperfections are unavoidable problems in structural fabrication, especially in the assembly of underwater structures. Figure 25 illustrates the equivalent creep strain of a structure with an initial geometric imperfection of 5‰Ri under the stress conditions of 30 MPa and 50 MPa. Initial geometric imperfection has no

appreciable impact on the structure at the stress levels of 30 MPa or 50 MPa. It can be seen that under loading conditions of the critical capacity, the influence of initial geometric imperfection with a value of 5‰Ri on the creep deformation of the structure is very small and can be ignored because the calculation in Section 4.2.2 shows that the maximum load capacity of the pressure-resistant structure under actual working conditions is 51.2 MPa.

The initial geometric imperfections in this section are made at 1 mm, 2 mm, 3 mm, and 4 mm, respectively, to further study its impact. The initial geometric imperfections of 2 mm and 4 mm under 50 MPa stress were determined, and the equivalent creep strain for each condition was compared as shown in Figure 26 in order to testify its impact under various loads. As seen in Figure 26, for an initial defect of 1–4 mm, all creep strains tend to converge, and the impact on the creep structure is negligible.

4.2.5. Effect of Temperature Field on Creep of the Pressure-Resistant Structure

The constitutive model of the material proposed for the present study can consider the effects of temperature considering the reality that the temperature during the diving of deep-sea equipment decreases to about 2°, which is much lower than the environmental temperature at sea surface. The equivalent creep strain results are shown in Figure 27. This study was conducted to verify the effect of temperature on seawater pressure and temperature, as indicated in Table 10 of Section 4.2.3. The same finite element calculations for various environmental temperatures under the outside pressure of 50 MPa are conducted in order to further confirm the impact of various load levels. The corresponding creep finite element simulation results are displayed in Figure 27. The temperature field for metals and alloys in the range of 30~2° can be regarded as the room temperature range, which has negligible effects on their creep deformation.

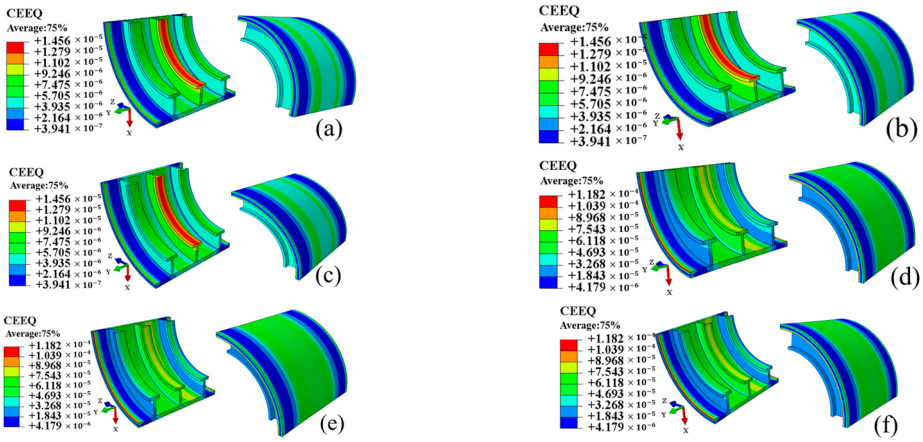

Figure 27. Equivalent creep for different temperature fields: (**a**) 2°, 30 MPa; (**b**) 2~30°, 30 MPa; (**c**) 30~2°, 30 MPa; (**d**) 2°, 50 MPa; (**e**) 2~30°, 50 MPa; (**f**) 30~2°, 50 MPa.

In the actual application, the diving velocity of the deep-sea equipment is low and the equipment maintains working status underwater for a relatively long time, according to the service requirement. From the calculations above, the designed pressure-resistant structure's overall creep deformation under certain environmental temperature fields and load levels will not have a significant impact on the structure's service ability.

5. Summary and Conclusions

Due to the long-term underwater loading of the pressure-resistant structure, the cold retention phenomenon (i.e., the room-temperature creep phenomenon) will occur. In the present study, the creep deformation of a pressure-resistant structure made of dissimilar titanium alloys is investigated. According to the experimental data, under different peak stresses on material specimens, an improved constitutive model is proposed and validated to well describe the behavior of Ti-6Al-4V and Ti-4Al-2V titanium alloys. Based on that,

the Fortran subroutine is compiled and applied to a finite element simulation of the creep deformation of the pressure-resistant structure with a convergence analysis on multiple sets of variables carried out first. Accordingly, the changing tendency of creep deformation with loading conditions, the initial status of the structure and the temperature field are obtained.

Aiming at the working condition of 3000 m depth, the total deformation of 1 year is very small comparing to the radius of the cylindrical structure according to finite element simulation. Therefore, in the structural design, the creep deformation of the pressure-resistant structure can be selectively considered as the tolerance range of design and manufacture, and the elastic strain range of the structure is retained at about 2 mm to ensure the normal operation of the submersible.

The present research offers a thorough understanding of the plastic deformation observed at room temperature in pressure-resistant structures made from titanium alloys, providing insightful advice for improving the design and dependability of submersible structures in challenging deep-sea environments.

Author Contributions: Conceptualization, funding acquisition, methodology, project administration, supervision, writing—review and editing: F.W.; data curation, investigation, software, writing—original draft: Z.L.; formal analysis, investigation: O.G.; data curation, validation: B.Z.; investigation, validation: J.Z.; resources, software: Z.S.; data curation: K.W. All authors have read and agreed to the published version of the manuscript.

Funding: This research is supported by the National Natural Science Foundation of China (Grant No. 52371282).

Institutional Review Board Statement: Not applicable.

Informed Consent Statement: Not applicable.

Data Availability Statement: Data will be made available on request.

Acknowledgments: The authors would like to express their gratitude for the support of the Fishery Engineering and Equipment Innovation Team of Shanghai High-Level Local University.

Conflicts of Interest: The authors declare no conflicts of interest.

References

1. Liu, T. Research on the design of spherical pressure hull in manned deep-sea submersible. *Chuanbo Lixue (J. Ship Mech.)* **2007**, *11*, 214–220.
2. Chausov, M.; Pylypenko, A.; Berezin, V.; Volyanska, K.; Maruschak, P.; Hutsaylyuk, V.; Markashova, L.; Nedoseka, S.; Menou, A. Influence of dynamic non-equilibrium processes on strength and plasticity of materials of transportation systems. *Transport* **2018**, *33*, 231–241. [CrossRef]
3. Xi, G.; Lei, J.; Qiu, J.; Ma, Y.; Yang, R. A semi-quantitative explanation of the cold dwell effect in titanium alloys. *Mater. Des.* **2020**, *194*, 108909. [CrossRef]
4. Kumar, J.; Singh, A.; Raman, S.G.S.; Kumar, V. Microtexture analysis and modeling of ambient fatigue and creep-fatigue damages in Ti-6Al-4V alloy. *Metall. Mater. Trans. A* **2017**, *48*, 648–658. [CrossRef]
5. Tympel, P.; Lindley, T.; Saunders, E.; Dixon, M.; Dye, D. Influence of complex LCF and dwell load regimes on fatigue of Ti–6Al–4V. *Acta Mater.* **2016**, *103*, 77–88. [CrossRef]
6. Fernandes, M.F.; de Oliveira Velloso, V.M.; Voorwald, H.J.C. Investigation of the damage and fracture of Ti-6Al-4V titanium alloy under dwell-fatigue loadings. *Procedia Struct. Integr.* **2022**, *35*, 141–149. [CrossRef]
7. Wang, F.; Cui, W. Experimental investigation on dwell-fatigue property of Ti–6Al–4V ELI used in deep-sea manned cabin. *Mater. Sci. Eng. A* **2015**, *642*, 136–141. [CrossRef]
8. Ma, X.; Li, F.; Zhao, C.; Zhu, G.; Li, W.; Sun, Z.; Yuan, Z. Indenter load effects on creep deformation behavior for Ti-10V-2Fe-3Al alloy at room temperature. *J. Alloys Compd.* **2017**, *709*, 322–328. [CrossRef]
9. Kirane, K.; Ghosh, S. A cold dwell fatigue crack nucleation criterion for polycrystalline Ti-6242 using grain-level crystal plasticity FE model. *Int. J. Fatigue* **2008**, *30*, 2127–2139. [CrossRef]
10. Gerland, M.; Lefranc, P.; Doquet, V.; Sarrazin-Baudoux, C. Deformation and damage mechanisms in an α/β 6242 Ti alloy in fatigue, dwell-fatigue and creep at room temperature. Influence of internal hydrogen. *Mater. Sci. Eng. A* **2009**, *507*, 132–143. [CrossRef]
11. Wang, F.; Sun, Z.; Liu, Z.; Hai, M.; Wu, Y.; Zhang, J.; Luo, R. Performance analysis on welded joints made of TC4/TA17 dissimilar titanium alloys. *Ocean Eng.* **2024**, *294*, 116758. [CrossRef]

12. Ou, P.; Cao, Z.; Hai, M.; Qiang, J.; Wang, Y.; Wang, J.; Zheng, G.; Zhang, J. Microstructure and mechanical properties of K-TIG welded dissimilar joints between TC4 and TA17 titanium alloys. *Mater. Charact.* **2023**, *196*, 112644. [CrossRef]
13. Betten, J. *Creep Experiments*; Springer Science & Business Media: Berlin/Heidelberg, Germany, 2002; pp. 245–255.
14. Bache, M. A review of dwell sensitive fatigue in titanium alloys: The role of microstructure, texture and operating conditions. *Int. J. Fatigue* **2003**, *25*, 1079–1087. [CrossRef]
15. Peng, J.; Zhou, C.-Y.; Dai, Q.; He, X.-H. Dwell fatigue and cycle deformation of CP-Ti at ambient temperature. *Mater. Des.* **2015**, *71*, 1–16. [CrossRef]
16. Evans, W.; Bache, M. Dwell-sensitive fatigue under biaxial loads in the near-alpha titanium alloy IMI685. *Int. J. Fatigue* **1994**, *16*, 443–452. [CrossRef]
17. Chandravanshi, V.; Prasad, K.; Singh, V.; Bhattacharjee, A.; Kumar, V. Effects of α + β phase deformation on microstructure, fatigue and dwell fatigue behavior of a near alpha titanium alloy. *Int. J. Fatigue* **2016**, *91*, 100–109. [CrossRef]
18. Kassner, M.; Kosaka, Y.; Hall, J. Low-cycle dwell-time fatigue in Ti-6242. *Metall. Mater. Trans. A* **1999**, *30*, 2383–2389. [CrossRef]
19. Zeng, W.; Zhou, Y. The influence of microstructure on dwell sensitive fatigue in Ti–6.5 Al–3.5 Mo–1.5 Zr–0.3 Si alloy. *Mater. Sci. Eng. A* **2000**, *290*, 33–38. [CrossRef]
20. Chen, K.; Yu, J.; Liu, Y.; Song, M.; Jiang, Q.; Ji, H.; Zou, J.; Zhang, Y.; Wang, H. Creep deformation and its correspondence to the microstructure of different polyester industrial yarns at room temperature. *Polym. Int.* **2019**, *68*, 555–563. [CrossRef]
21. Kale, C.; Srinivasan, S.; Hornbuckle, B.C.; Koju, R.K.; Darling, K.; Mishin, Y.; Solanki, K.N. An experimental and modeling investigation of tensile creep resistance of a stable nanocrystalline alloy. *Acta Mater.* **2020**, *199*, 141–154. [CrossRef]
22. Yuhao, G.; Gang, L.; Yi, H. A complemented multiaxial creep constitutive model for materials with different properties in tension and compression. *Eur. J. Mech.-A/Solids* **2022**, *93*, 104510.
23. Raman, V.; Berriche, R. An investigation of the creep processes in tin and aluminum using a depth-sensing indentation technique. *J. Mater. Res.* **1992**, *7*, 627–638. [CrossRef]
24. Mahmudi, R.; Roumina, R.; Raeisinia, B. Investigation of stress exponent in the power-law creep of Pb–Sb alloys. *Mater. Sci. Eng. A* **2004**, *382*, 15–22. [CrossRef]
25. Ahmed, R.; Barrett, P.R.; Hassan, T. Unified viscoplasticity modeling for isothermal low-cycle fatigue and fatigue-creep stress–strain responses of Haynes 230. *Int. J. Solids Struct.* **2016**, *88*, 131–145. [CrossRef]
26. Ahmed, R.; Barrett, P.R.; Menon, M.; Hassan, T. Thermo-mechanical low-cycle fatigue-creep of Haynes 230. *Int. J. Solids Struct.* **2017**, *126*, 90–104. [CrossRef]
27. Ahmed, R.; Hassan, T. Constitutive modeling for thermo-mechanical low-cycle fatigue-creep stress–strain responses of Haynes 230. *Int. J. Solids Struct.* **2017**, *126*, 122–139. [CrossRef]
28. JianPing, J.; Guang, M.; Yi, S.; SongBo, X. An effective continuum damage mechanics model for creep–fatigue life assessment of a steam turbine rotor. *Int. J. Press. Vessel. Pip.* **2003**, *80*, 389–396. [CrossRef]
29. Liu, N.; Dai, H.; Xu, L.; Tang, Z.; Li, C.; Zhang, J.; Lin, J. Modeling and effect analysis on crack growth behavior of Hastelloy X under high temperature creep-fatigue interaction. *Int. J. Mech. Sci.* **2021**, *195*, 106219. [CrossRef]
30. Tinga, T.; Brekelmans, W.; Geers, M. Time-incremental creep–fatigue damage rule for single crystal Ni-base superalloys. *Mater. Sci. Eng. A* **2009**, *508*, 200–208. [CrossRef]
31. Shi, S.; Deng, Q.; Zhang, H.; Feng, L.; Xu, X.; Ding, J.; Chang, H.; Zhou, L. Microstructure stability and damage mechanisms in an α/β Ti-6Al-4V-0.55 Fe alloy during low cycle dwell-fatigue at room temperature. *Int. J. Fatigue* **2022**, *155*, 106585. [CrossRef]
32. Kumar, J.; Rao, A.V.; Raman, S.G.S.; Kumar, V. Creep-fatigue damage simulation at multiple length scales for an aeroengine titanium alloy. *Int. J. Fatigue* **2018**, *116*, 505–512. [CrossRef]
33. Liu, Z.; Gaidai, O.; Sun, J.; Xing, Y. Deconvolution approach for floating wind turbines. *Energy Sci. Eng.* **2023**, *11*, 2742–2750. [CrossRef]
34. *GB/T 2039—2012*; Metallic materials-Uniaxial Creep Testing Method in Tension. Standards Press of China: Beijing, China, 2012.
35. *ASTM E139-11*; Standard Method for Conducting Creep, Creep-Rupture, and Stress-Rupture Tests of Metallic Materials, Annual Book of ASTM Standards. ASTM International: West Conshohocken, PA, USA, 2011.